

MEMS Modelling in the Context of Inertial Navigation

Jerzy Demkowicz

Abstract—Underwater navigation is a research topic current undertaken in many areas of underwater research. The article presents an analysis resulting from MEMS modelling in the context of inertial navigation. The ideal approach was confronted with its limitations, but a non-linear approach, close to the real one, was also presented. Both models were compared in the context of inertial navigation. Random disturbances and their impact on linear and nonlinear dynamic systems, and in this context on Brownian noise motion, were also analysed. The linear velocity and displacement estimates generated by the presented models were compared to the ideal responses. The phenomenon of bifurcation in the context of inertial measurements is presented. Some of the analysis is performed on real data, but for greater clarity, some is performed on simulated data to highlight design issues and limitations.

Keywords—MEMS; model; accelerometer; nonlinear; limitations; inertial navigation

I. INTRODUCTION

INERTIAL navigation (INS) works based on Newton's first law, also called the law of inertia. INS is based on the double integration of acceleration:

$$d(t) = \iint (a(t)) dt \quad (1)$$

where:

d – distance,

a – true acceleration from acceleration sensor,

t – time.

The key advantage of inertial navigation is its autonomy, but also its passivity [1],[2],[3]. We use real sensors or accelerometers for measurements, so deterministic errors must be taken into account: errors that can be corrected based on the dynamics of the system using a set of calibration tests, and non-deterministic errors.

$$d(t) = \iint (a(t) + a_n(t)) dt \quad (2)$$

where:

a_n —acceleration noise.

The problem in this case is a_n errors, which come from two sources: external and internal factors, such as temperature and pressure. They are described using the Allan variance. The measurement errors are then integrated, leading to drift over time. This means that errors accumulate over time. Some of the external errors are eliminated by using a hermetically sealed IMU (inertial measurement unit) in a vacuum to minimise the

influence of pressure and temperature, and regular calibration is applied (including vacuum checking) [4], [5],[6].

However, when modelling INS errors, sensor nonlinearity and the gravity model must also be taken into account because gravity measurement error is an important factor affecting the performance of INS systems.

The implementation of an inertial frame is difficult mainly due to the problem of actually using the law of inertia, because the measurement of acceleration requires the use of gravitational mass (proof mass of the mass-spring-damper system) and due to the equivalence principle (general relativity). The topic is relatively new, probably novel and is somehow connected to [7],[8], which are also relatively new papers that deal with the bifurcation problem in MEMS systems, but do not deal with this problem in the context of INS systems. The results of this paper can be used in the design process of INS systems.

The first section of the article presents a short description of interferences affecting the final measurements. Section 3 presents of the method of filtering these interferences, while Sections 4 and 5 describe problems that arise when using even ideal MEMS sensors. The article ends with a summary.

II. ERRORS IN INERTIAL SYSTEMS

MEMS accelerometers are very small, typically just a few millimetres in size. MEMS are manufactured using semiconductor manufacturing processes, so they have very low power consumption, making them ideal for battery-powered applications. MEMS accelerometers and gyroscopes have many advantages and are widely used in various applications [9],[10].

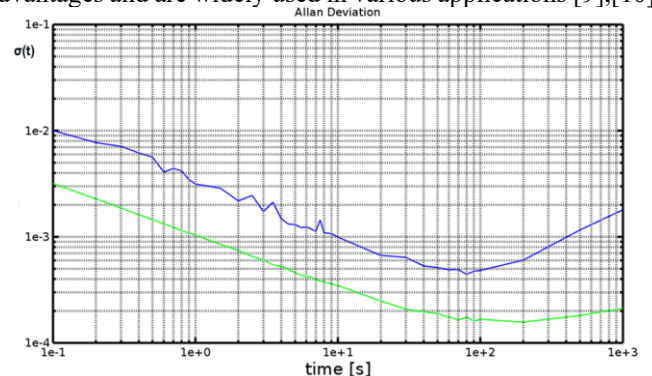


Fig. 1. Accelerometer Allan variance log-log plots of MEMS IMU array (green) vs. single MEMS IMU (blue) [11].

However, MEMS errors in the form of accelerometer systematic error, gyroscope and accelerometer random errors,

scale factors, and nonlinearity errors are still difficult to overcome [12].

Random errors do not result directly from the dynamics of the MEMS system. Their estimation depends on knowledge of the sensor noise model [13]. Simple Allan variance provides a means of identifying and quantifying various noise and error terms that exist in the data [11,14], as presented in Fig. 1.

For instance, the in-run bias stability standard deviation error references the minima of the Allan deviation curve, as presented in Fig. 1 for the data from an IMU array and for a single IMU in static conditions. Using an IMU array is one way to improve accelerometer and gyroscope measurements [11].

The Allan variance is proportional to the total noise power of the sensor output passing through the bandpass filter. This filter depends on the sampling rate, so one can study different types of random processes by adjusting the correlation time. The results for the MEMS gyroscope are similar to the results presented in Fig. 1 [11].

A. Gyro Bias

The gyro bias error is the main contributor, though other factors, such as accelerometer bias and noise, are also important in the error budget. Due to gyroscope measurement errors, there are errors in the measurement of the actual (true) plumb line (G), as shown in Fig. 2. Even small errors in the tilt IMU measurement have serious consequences in the context of inertial navigation. Fig. 2 presents the pitch with the bias Δ .

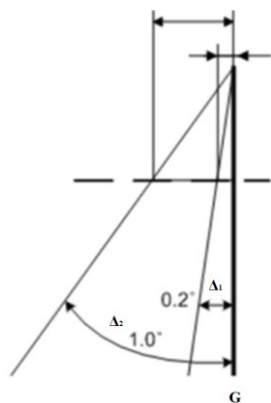


Fig. 2. Differences in roll measurements for IMUs

It is enough that the angle measurement system has an error of 0.2 degrees and a linear acceleration error of $0.034 \frac{m}{s^2}$. This is a lot, because after 10 seconds, the error in determining the position will be 1.7 m. A constant bias Δ in accelerometer measurements, as presented in Fig. 2, propagates into velocity and finally position errors, because the gyro bias is first integrated into attitude errors. Distance errors increase proportionally to t^3 due to gyroscopic errors and proportionally to t^2 due to errors in accelerometer measurements. When an attitude/tilt deviation Δ occurs, it is included in the final sensor output, which is then double integrated. This leads to a cubic increase in final distance error due to the tilt. This error increases proportionally with t^3 . This is a serious problem, and gyroscopic error can be considered the main cause of errors in the context of INS measurements.

B. Gyro Brownian Motion

Angle measurement error is usually characterised by a random angular error that accumulates over time. This is often referred to as a random walk, Fig. 3. So, the tilt (pitch, roll) bias changes over time.

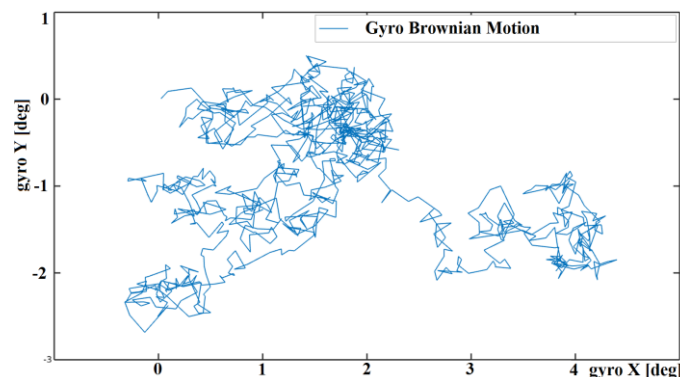


Fig. 3. Brownian motion of Gyro ARX-ARY

If we take into account the gyro in 2D —the second dimension—i.e. angular rate/velocity X (ARX) and angular rate Y (ARY), we will get a typical example of Brownian motion over time, as presented in Fig. 3.

B. Other Error Sources

Other sources of sensor-related errors that contribute to inertial measurement errors include scale factor error, sensor nonlinearity errors, and associated g-sensitive errors. However, there are also two important error sources that are not related to sensor imperfections. One of them is an error in the sensor installation. Gravity modelling errors is the other one, especially for precise INS positioning. There are also errors due to the Shuler effect, however these are beyond the scope of this article.

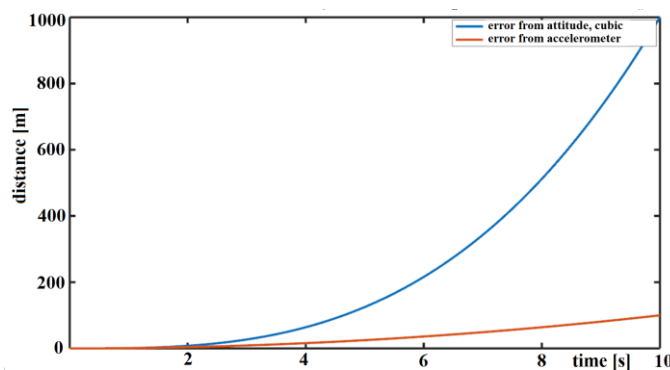


Fig. 4. Errors proportional to cubic (blue), quadratic (red)

These considerations show that accelerometer and gyroscope drift lead to an indeterminate increase in INS navigation result errors. This can be approximated using polynomials: e.g., t^2 and t^3 , as presented in Fig.4. In summary, gyroscope bias is the most important contributor to the INS error budget, while the contribution of other error sources is approximately an order of magnitude lower.

III. KALMAN FILTER APPROACH TO TILT EVALUATION

As mentioned above, the tilt measurement error is the main error factor in INS. One could try to calculate tilt from the accelerometer, but it produces measurements with large errors caused by the pitch calculation due to the inverse problem (see Equation 3). For pitch, it is as follows:

$$p_{meas} = atan \frac{a_x + a_{x_b}}{\sqrt{(a_y + a_{y_b})^2 + (a_z + a_{z_b})^2}} \quad (3)$$

where:

a_x, a_{x_b} —acceleration and bias in the x direction of the IMU frame,

$a_y + a_{y_b}$ —acceleration and bias in the y direction of the IMU frame,

$a_z + a_{z_b}$ —acceleration and bias in the z direction of the IMU frame.

However, Fig. 5 shows distortions (sharp jumps, pitch amplitudes), besides linear acceleration.

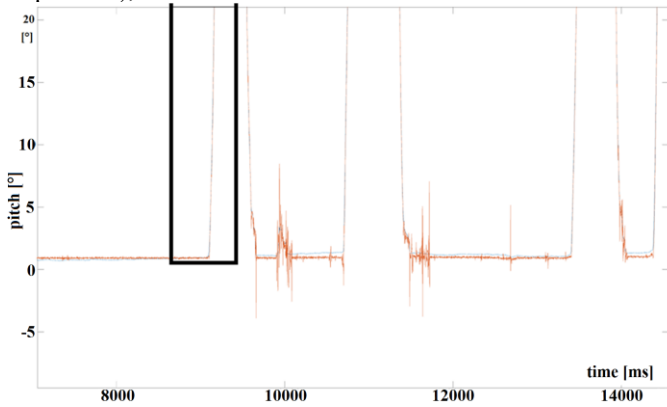


Fig. 5. Pitch measurement using accelerometer

Similarly in Fig. 6, the red line is the pitch calculated from the accelerometer (red—unstable measurement) and is an enlarged fragment of Fig. 5, the blue line is the pitch calculated from the gyroscope. Now, the pitch calculated from the gyroscope (ARY) is more stable (blue) and it is clearly visible.

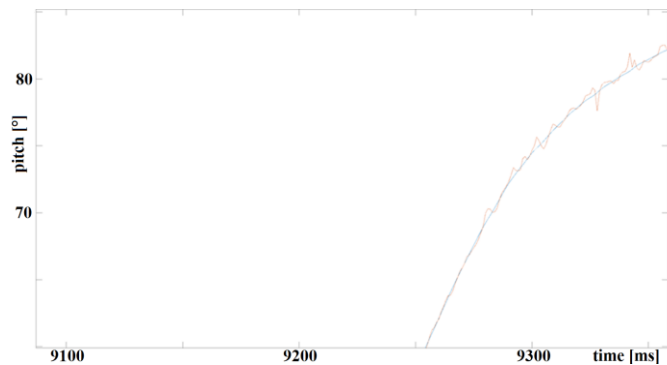


Fig. 6. Pitch measurement using accelerometer enlarged from Fig. 5

The gyroscope is insensitive to acceleration a . Unfortunately, the pitch from the gyro is burdened with slowly changing errors coming from bias error (blue in the Figs. 7 and 8).

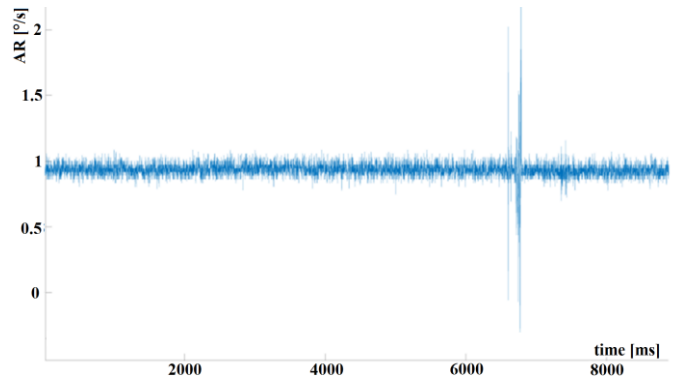


Fig. 7. Real data from gyro, slowly changing errors

This error is more easily visible in Fig. 8 over a longer period and in the presence of measurements using accelerometers. The most important feature of Fig. 8 is the gyro bias plot in blue.

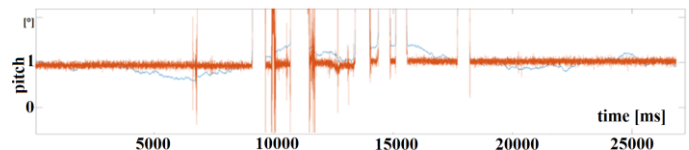


Fig. 8. Pitch measurement using accelerometer (red) and gyroscope (blue) with angle random walk (clearly observed in stationary measurement)

Angle Random Walk (pitch calculated from gyro) for stationary measurement is shown in black in Fig. 9 for the first 80 s, while pitch errors calculated from the accelerometer are shown in red, as presented in Fig. 8.

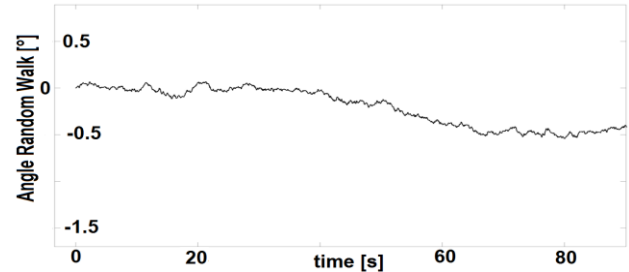


Fig. 9. Angle Random Walk process records for an Xsens MTi-G-28A53G35 for static measurements

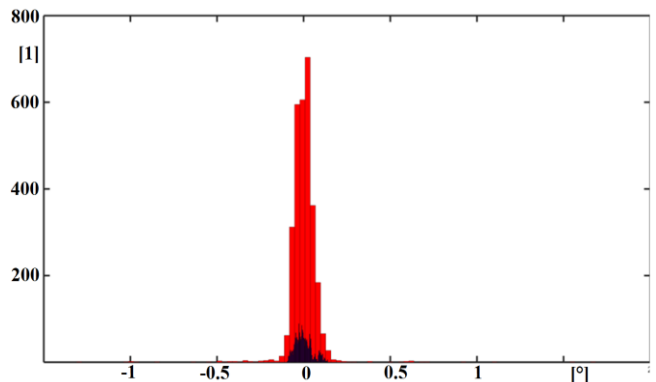


Fig. 10. Distribution of pitch calculated with accelerometer, in red; distribution of ARW (pitch distribution from gyro, after integration), in black

The distribution of this data is presented in Fig. 10. The distribution of the pitch from the accelerometer is shown in red in this figure, while the distribution of the ARW (Angle Random Walk, pitch distribution from gyro, after integration) is shown in black. From our point of view, the black distribution (ARW) is better than the red one because of the smaller standard error, which is the main reason why the Kalman filter works, as presented in Fig.11.

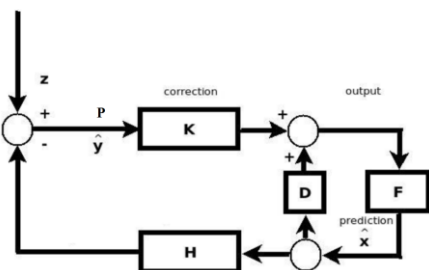


Fig. 11. Kalman fusion/filtering algorithm

where:

- output*—estimation vector,
- F*—state transition model,
- D*—delay,
- H*—observation model,
- K*—Kalman gain.

Te whole process is controlled by **P**—estimated covariance matrix [16],[17]. The overall process is depicted in [17],[18], however at this point, it is important to underline that the process uses stochastic properties of measurements from the sensors.

The above problems related to measurement noise can be partially solved by using a Kalman filter. The application of the Kalman approach works well in static or quasi-static conditions. That is, in the absence of external linear acceleration.

The question is: what about linear accelerations? This is a problem of the equivalence principle (G and linear/inertial acceleration) [1]. If we had an infinitely precise G and tilt measurement, we would be able to define the difference between the two. Linear acceleration is a real problem while determining tilt. Any MEMS using the Kalman algorithm shows nonsense measurements if we give it linear acceleration (it is enough to move the MEMS left, right), which is a serious drawback of the Kalman filter used in the context of tilt evaluation using MEMS, as shown in Fig. 12. In the intervals [1200–3000], Kaman’s responses are definitely incorrect, as presented in Fig. 12.

The point is that the Kalman approach is insufficient in the presence of linear accelerations, i.e. in dynamic conditions, i.e. it is enough to dynamically move the IMU device (left and right, up and down) and the tilt readings are completely disturbed. The Kalman response is highly distorted (green in Fig. 12). Fig. 12 shows the IMU in a static position for a maximum of 1.2 s, in motion for 1.2–1.4 s, and in a static position after 1.4 s, as seen from the accelerometer (red) and gyroscope (blue) readings, however the Kalman filter returns to its stable position only after 3 s. We can therefore say that the Kalman filter implemented in the IMU works only in conditions close to static.

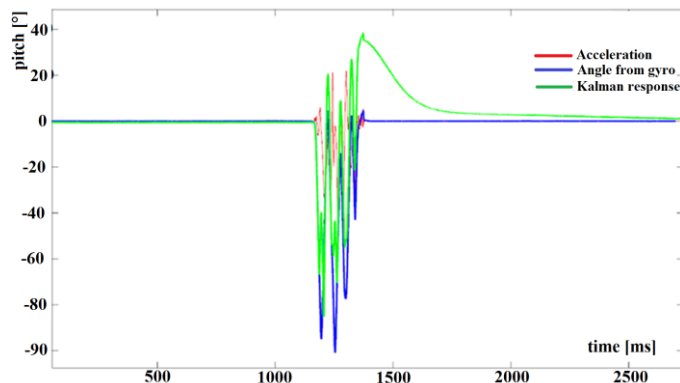


Fig. 12. Kalman output in dynamic conditions

Unfortunately, it turns out that the problem associated with this increases significantly in certain circumstances with changing external force, its dynamics, and frequency. An illustration of this is the following section, which presents the use of MEMS in conditions of a rapidly changing external forcing force.

IV. LINEAR PROOF MASS MOTION EQUATION FOR ACCELEROMETER SENSOR

The basic principle of operation of a Micro-Electro-Mechanical Systems (MEMS) accelerometer is based on the physical phenomenon of capacitance. The sensor consists of a small mass **m** suspended on springs, which move in response to acceleration forces, see Eq. 3. As the mass moves, the distance **x** between two plates changes, which alters the capacitance [19],[20]. This change in capacitance is then converted into a voltage signal that can be read by an electronic circuit.

The proof mass motion equation in an acceleration sensor is given by Eq. 4:

$$m \frac{\partial^2 x(t)}{\partial t^2} + D_o \frac{\partial x(t)}{\partial t} + kx(t) = F_o \tag{4}$$

where:

- m* - proof mass,
- D_o* - dumping coefficient,
- K* - spring constant, linear stiffness,
- F_o* - external forcing force.

This is a regular differential equation, and its solution is the solution to this equation, presented in Eq.5:

$$x(t) = c_1 e^{1/2t(-\sqrt{D_o^2 - 4km/m - \frac{D_o^2}{m}})} + c_2 e^{1/2t(\sqrt{D_o^2 - 4km/m - \frac{D_o^2}{m}})} + \frac{F_o}{k} \tag{5}$$

For the initial conditions: $x(t_0) = 0, \frac{\partial x(t_0)}{\partial t} = 0, \text{ and } t_0 = 0.$ The output from the accelerometer (ideal solution) is presented in Fig. 13. It is a response to rectangular acceleration excitation, i.e. accelerometer readings (red), blue (speed), and green (distance). Fig. 14 presents an enlargement from Fig. 13.

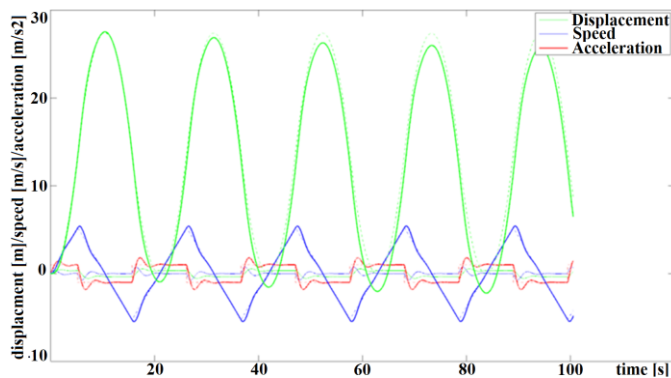


Fig. 13. Accelerometer response to rectangular excitation (acceleration—red, speed—blue, displacement—green)

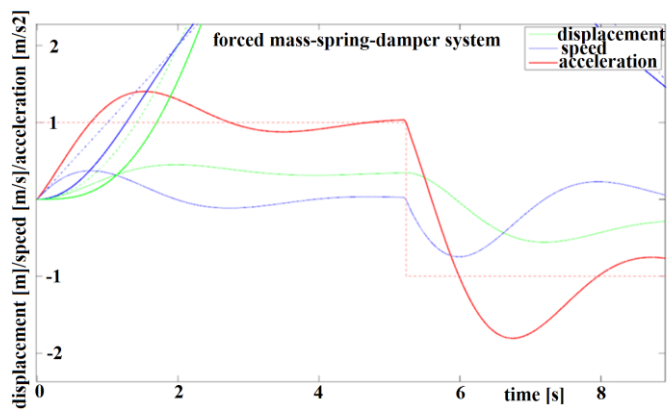


Fig. 14. Previous Fig. 13, enlarged

The dashed lines in Fig. 14 show the ideal responses, i.e. ideal acceleration (red dashed), ideal speed—integral of acceleration (blue dashed), distance—integral of velocity (green dashed). This is an illustration of the regular differential equation (Eq. 4 in the article). Even such an ideal approach causes errors, which can best be observed based on the calculated distance/displacement (Fig. 15).

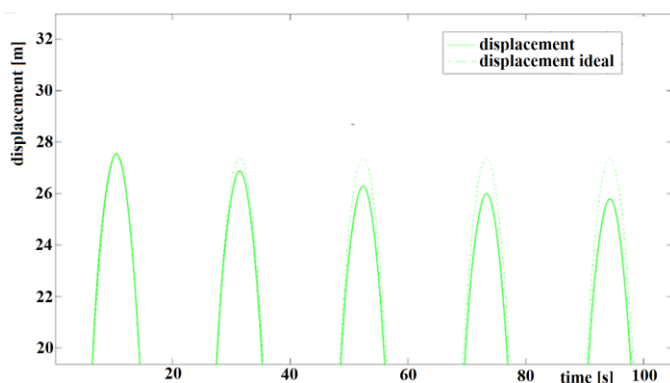


Fig. 15. Displacement for ideal accelerometer (green—true, dashed green—ideal)

It should produce the green dashed line (Fig. 15), however its output is as marked with the solid green line (Fig. 15). And unfortunately, it cannot get better. After several dozen seconds, differences of several metres can be observed (it depends on the time constant), as presented in Fig. 15.

V. NONLINEAR PROOF MASS MOTION EQUATION FOR ACCELEROMETER SENSOR

Unfortunately, there is another issue. Fig. 16 is analogous to Figs. 13, 14, but for the Duffing equation, i.e. an equation with only one non-linear element:

$$m \frac{\partial^2 x(t)}{\partial t^2} + D_o \frac{\partial x(t)}{\partial t} + kx(t) + \varepsilon x^3(t) = F_o \quad (6)$$

where:

m - proof mass,

D_o - damping coefficient,

k - spring constant, linear stiffness,

ε - nonlinearity controls the amount of non-linearity in the restoring force, nonlinear stiffness parameter,

F_o - external force,

ε , - epsilon is nonlinearity and controls the amount of non-linearity in the restoring force.

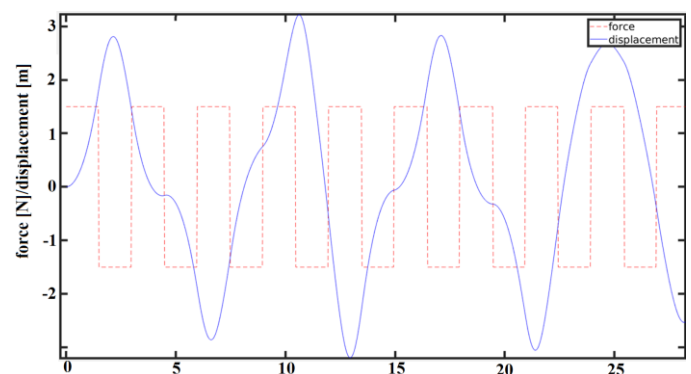


Fig. 16. Response of Duffing Eq. 3 on rectangular acceleration excitation

If epsilon, $\varepsilon = 0$, the Duffing equation describes a damped and driven simple harmonic oscillator. However, if damping $D_o=0.1$, stiffness $k=1$, nonlinearity $\varepsilon=0.3$, and periodic external forcing force F_o of $f = 1.5$ Hz, this leads to the phenomenon of bifurcation, as shown in the phase space diagram in Fig.17.

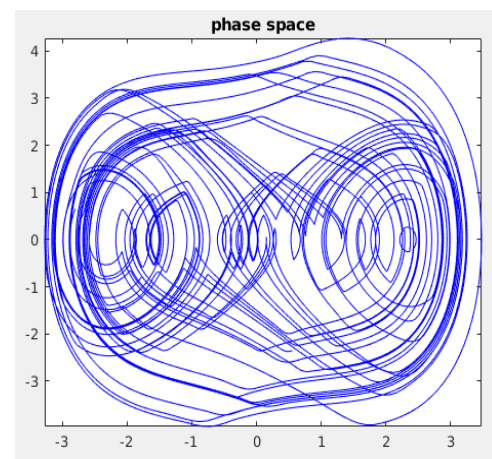


Fig. 17. Phase space diagram of Duffing equation

We get chaos and a strange attractor, as presented in Fig. 17, if the driving force is applied to the system. The Poincaré plots or Poincaré section is then a complicated curve (see Fig. 18).

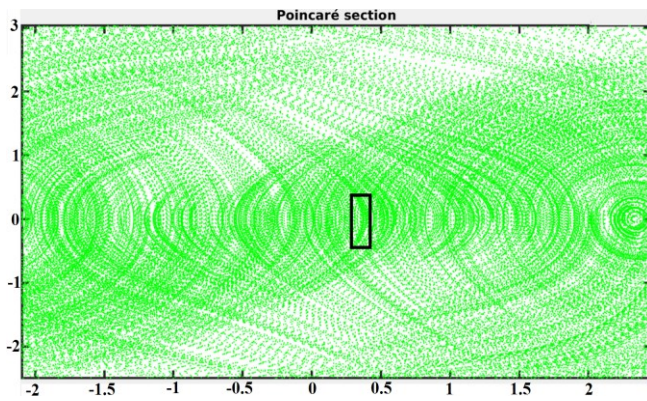


Fig. 18. Poincaré section as a complicated curve (strange attractor)

This diagram shows a strange attractor (Fig. 18). It is a limiting set of points to which the trajectory tends (after an initial unsteady period) during each period of the external driving force. The structure is not completely random. The black rectangle has been enlarged in Fig. 19 and the repeating structures presented in Fig. 18 can be observed in Fig. 19. Zooming in on the black box area in Fig. 18 reveals the same features that were present on a smaller scale in Fig. 19. It is a fractal.

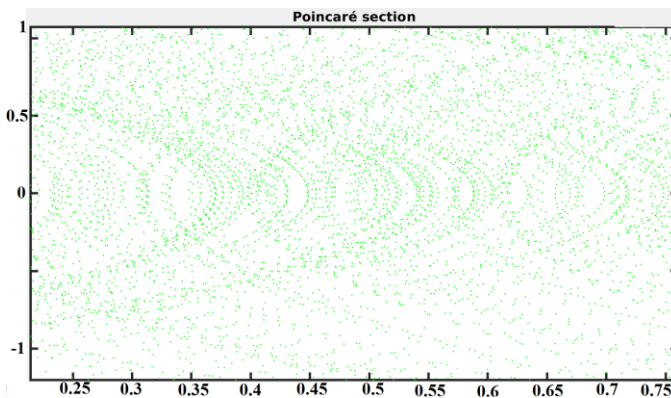


Fig. 19. Fig. 18, enlarged fragment

A characteristic feature of a fractal is the presence of the same features in different parts of the figure and at different scales.

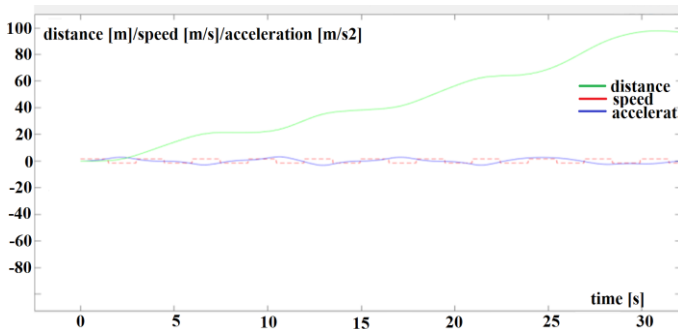


Fig. 20. Accelerometer response to rectangular excitation—bifurcation (acceleration—red, speed—blue, displacement—green), analogous to Fig. 13

In Fig. 20, it is the distance (green) calculated for this particular case of the Duffing equation (slightly nonlinear equation), whose error becomes huge after a few seconds.

Similarly to Fig. 13, the distance measurement in this case has a very large error (Fig. 20), which shows how important the dynamics (amplitude range) and frequency of the forcing force are for the operation of the IMU and, consequently, the appropriate design of the system for the operating conditions. It should be noted that the frequency at which the bifurcation phenomenon occurs is only 1.5 Hz, but even without this phenomenon, when using linear subsystems, the measured and theoretical distances differ significantly, and this depends on the conditions in which the device operates.

CONCLUSION

Measuring displacement or distance using inertial sensors is not only subject to errors related to external disturbances from the environment, such as temperature, pressure, etc. Even if we used ideal sensors, we would have to take into account errors resulting from the high frequency of excitation. Of course, non-linear sensor models worsen these situations and, in some cases, may lead to the bifurcation phenomenon, which significantly worsens and disturbs the measurement of the distance travelled. The article presents problems resulting from the use of MEMS sensors in an ideal situation and when nonlinearity is taken into account. Nonlinearity problems occur in dynamic conditions and are easy to observe using IMUs using Kalman filters. When inertial models are used, the quality of sensor operation depends on the excitation frequency and nonlinearity. The same applies to the consideration of non-linear phenomena. In the latter case, however, the measurement deteriorates significantly, due to bifurcation. This should be taken into account when designing acceleration sensors used in dynamic conditions.

REFERENCES

- [1] Groves, P. D., Principles of GNSS, Inertial, and Multisensor Integrated Navigation Systems, Artech House, London, 2013.
- [2] Paull L., Saeedi S., Seto M., Li H., AUV Navigation and Localization: A Review, IEEE Journal of Oceanic Engineering, Vol. 39, No. 1, January 2014.
- [3] Demkowicz, J., Autonomous Vehicle Navigation in Dense Urban Area in Global Positioning Context, 2018 11th International Conference on Human System Interaction (HSI), IEEE Xplore: 2018.
- [4] Kongsberg Seatex MRU-5 Manual, Copyright © Kongsberg Seatex AS 2008.
- [5] Quick Start Guide to the 3DMGX3 Soft & Hard Iron Calibration, www.microstrain.com
- [6] IEEE Recommended Practice for Inertial Sensor Test Equipment Instrumentation Data Acquisition and Analysis. Available online: <https://ieeexplore.ieee.org/servlet/opac?punumber=10423> (accessed on 31 March 2011).
- [7] Qiao Y., Shi Z., Xu Y., Wei X., Elhady A., Abdel-Rahman E., Huan R., Zhang W., Frequency unlocking-based MEMS bifurcation sensors. Nature, Microsystems & Nanoengineering volume 9(58), Article number: 58, 2023.
- [8] Vamsi C. Meesala, Muhammad R. Hajj, Eihab Abdel-Rahman, Bifurcation-based MEMS mass sensors, International Journal of Mechanical Sciences Volume 180, 15 August 2020, 105705.
- [9] Prikhodko, I. P., Bearss, B., Merritt, C., Bergeron, J., Blackmer, C. Towards self-navigating cars using MEMS IMU: Challenges and opportunities. In Proceedings of the 2018 IEEE International Symposium on Inertial Sensors and Systems (INERTIAL 2018), Lake Como, Italy, 26–29 March 2018, pp. 1–4.
- [10] Łoziński, P., Demkowicz, J., Proof of Concept of Indoor Location System Using Long RFID Readers and Passive Tags, Springer monography 2022, https://doi.org/10.1007/978-981-19-6004-8_51

- [11] Demkowicz, J., Bikonis, K., Study of Array of MEMS Inertial Measurements Units Under Quasi-Stationary and Dynamic Conditions, Polish Maritime Research [ISSN: 1233-2585].
- [12] Shultz Kenneth, S. Measurement Theory in Action, Taylor & Francis Ltd.: 2020.
- [13] Kovacic, I., Brennan, M. J. The Duffing Equation: Nonlinear Oscillators and Their Behaviour. John Wiley & Sons, Hoboken. <https://doi.org/10.1002/9780470977859>
- [14] Tahmineh Azizi, Gabriel Kerr, Application of Stability Theory in Study of Local Dynamics of Nonlinear Systems, Journal of Applied Mathematics and Physics, Vol.8 No.6, June 23, 2020.
- [15] Woodman, O. J., An introduction to inertial navigation, August 2007, University of Cambridge.
- [16] Yeong J., Velasco-Hernandez G., Barry J., Walsh J., Sensor and Sensor Fusion Technology in Autonomous Vehicles: A Review, Sensors 2021, 21(6), 2140, <https://doi.org/10.3390/s2106214>
- [17] Brown, R. G., Hwang, P. Y. C. Introduction to Random Signals and Applied Kalman Filtering with MATLAB Exercises, 3rd., John Wiley & Sons Inc.: New York, NY, USA, 1997.
- [18] Demkowicz, J. MEMS Gyro in the Context of Inertial Positioning. In Proceedings of the 2017 Baltic Geodetic Congress (BGC Geomatics), Gdansk, Poland, 22–25 June 2017, pp. 247–251.
- [19] Quinchia A. G., Falco, G., Falletti E., DAVIS F., Ferrer, C., A Comparison between Different Error Modeling of MEMS Applied to GPS/INS Integrated Systems, Sensors 2013, 13(8), 9549–9588, <https://doi.org/10.3390/s130809549>
- [20] Poddar, S., Kumar, A. Scale-free PSO for in-run and infield inertial sensor calibration. Measurement 2019, 147, 106849.